

Mechanics of head fold formation: investigating tissue-level forces during early development

Victor D. Varner¹, Dmitry A. Voronov^{1,2} and Larry A. Taber^{1,*}

SUMMARY

During its earliest stages, the avian embryo is approximately planar. Through a complex series of folds, this flat geometry is transformed into the intricate three-dimensional structure of the developing organism. Formation of the head fold (HF) is the first step in this cascading sequence of out-of-plane tissue folds. The HF establishes the anterior extent of the embryo and initiates heart, foregut and brain development. Here, we use a combination of computational modeling and experiments to determine the physical forces that drive HF formation. Using chick embryos cultured ex ovo, we measured: (1) changes in tissue morphology in living embryos using optical coherence tomography (OCT); (2) morphogenetic strains (deformations) through the tracking of tissue labels; and (3) regional tissue stresses using changes in the geometry of circular wounds punched through the blastoderm. To determine the physical mechanisms that generate the HF, we created a three-dimensional computational model of the early embryo, consisting of pseudoelastic plates representing the blastoderm and vitelline membrane. Based on previous experimental findings, we simulated the following morphogenetic mechanisms: (1) convergent extension in the neural plate (NP); (2) cell wedging along the anterior NP border; and (3) autonomous in-plane deformations outside the NP. Our numerical predictions agree relatively well with the observed morphology, as well as with our measured stress and strain distributions. The model also predicts the abnormal tissue geometries produced when development is mechanically perturbed. Taken together, the results suggest that the proposed morphogenetic mechanisms provide the main tissue-level forces that drive HF formation.

KEY WORDS: Biomechanics, Chick embryo, Computational modeling, Convergent extension, Morphogenesis, Optical coherence tomography

INTRODUCTION

The early metazoan embryo is constructed primarily out of thin epithelia (Davies, 2005). During morphogenesis, these two-dimensional (2D) epithelial sheets are shaped (through a series of folds and in-plane deformations) into the complex 3D structures that make up the embryonic body plan. Physical forces play an indispensable role in this process, and recent work has shown that mechanical loads can influence gene expression patterns during development (Farge, 2003; Desprat et al., 2008; Wozniak and Chen, 2009). Although much work has been done to identify precursor cell populations and follow their differentiation into specific tissues, relatively few investigations have quantified the tissue deformations involved in early embryogenesis or identified the mechanical forces that drive them (Hutson et al., 2003; Zamir et al., 2005; Rauzi et al., 2008; Blanchard et al., 2009).

Here, we address the mechanics of head fold (HF) formation in the early chick embryo (Fig. 1). This crescent-shaped fold, which is conserved across amniotes and mammals, forms at the anterior end of the neural plate (NP) and constitutes the first body fold. It initiates brain, foregut and heart development (Bellairs, 1953; Stalsberg and DeHaan, 1969; Schoenwolf and Smith, 2000) and is the first major 3D structure to form in the chick embryo. The biophysical mechanisms that drive HF formation remain poorly understood.

In this paper, we combine computational modeling with data obtained from experiments on chick embryos to investigate the mechanical forces that shape the HF. Mathematical models offer particular insight here, allowing us to test whether a given set of forces could plausibly generate the tissue deformations observed during morphogenesis. Our results indicate that a combination of the following morphogenetic processes is likely to drive HF formation: (1) convergent extension within the NP; (2) coordinated, active cell wedging at the anterior NP border; and (3) epidermal shaping outside the NP. Our approach can be readily generalized to other morphogenetic processes and offers insight into how forces are organized at the tissue level to create biological form.

MATERIALS AND METHODS

Experimental methods

Embryo preparation and culture

Fertilized White Leghorn chicken eggs were incubated in a humidified, forced draft incubator at 38°C for 23–29 hours to yield embryos between Hamburger and Hamilton (HH) stages 5 and 7 (Hamburger and Hamilton, 1951). Whole embryos were harvested using a filter paper carrier method (Voronov and Taber, 2002). The embryo and underlying vitelline membrane (VM) were kept intact, thereby preserving the stresses normally present in the tissue. To remove the effects of surface tension, each embryo was completely submerged under a thin layer of liquid culture media and incubated at 38°C in 95% O₂ and 5% CO₂ (Voronov and Taber, 2002).

Manipulation of embryos

Endoderm and mesoderm were removed from a group of HH stage 5 embryos ($n=6$) to determine whether the forces behind HF formation are ectodermal in origin. Small amounts (~1 nl) of 3–5% collagenase in PBS were injected between the ectoderm and endo/mesoderm using pulled glass micropipettes and a pneumatic pump (PicoPump PV830, World Precision Instruments). Embryos were incubated at 38°C for 30 minutes, and the endo/mesoderm removed using glass needles.

¹Department of Biomedical Engineering, Washington University, St Louis, MO 63130, USA. ²Institute for Information Transmission Problems, Russian Academy of Sciences, Moscow 127994, Russia.

* Author for correspondence (lat@wustl.edu)

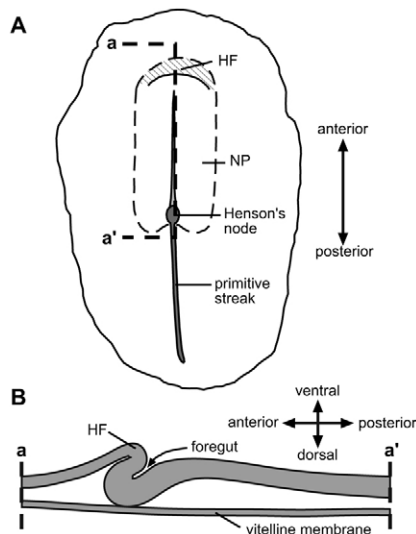


Fig. 1. The head fold (HF) is the first major 3D structure to form in the chick embryo. (A) Schematic ventral view of HH stage 7 embryo. The crescent-shaped HF forms at the anterior end of the neural plate (NP). Prior to HF formation, the chick blastoderm is approximately planar. (B) Sagittal view of midline section a-a' in A. The blastoderm is in local contact with the vitelline membrane (VM) and doubled over into an S-shaped configuration.

To perturb normal development, the VM was removed or the blastoderm was cut to relieve tissue stresses. Each microsurgery was performed under a dissecting microscope using needles fashioned from pulled glass micropipettes.

Optical coherence tomography (OCT)

OCT was used to obtain 3D images of living embryos; its depth of field (~2 mm) and spatial resolution (~10 μm) are well suited for this purpose (Huang et al., 1991; Fujimoto, 2003). Cross-sectional image stacks were reconstructed into 3D volumes and optically sectioned using Volocity (Improvision, Waltham, MA, USA). Time-lapse experiments were conducted with the custom-built OCT system described previously (Filas et al., 2007; Filas et al., 2008).

Tissue stress estimates

Machined glass micropipettes were used to excise circular plugs of tissue from HH stage 4 ($n=3$) and stage 6 ($n=9$) embryos. Bright-field images of each wounded embryo were captured with a dissecting microscope (Leica MZ8) and attached video camera. Approximately 30–45 seconds elapsed between wounding and image capture. To rule out the possibility that our results were affected by a healing response, as has been reported in embryos at approximately comparable developmental stages (Clark et al., 2009; Joshi et al., 2010), we stained F-actin using Rhodamine-phalloidin (Molecular Probes, Eugene, OR, USA). These experiments confirmed that an intact contractile ring had not yet assembled around the wounds (V.D.V., unpublished).

As described by Varner and Taber (Varner and Taber, 2010), wound geometry was used to characterize regional tissue stress (force per unit area). For each wound, the Analyze Particles routine in ImageJ (NIH) was used to determine the area, major axis (a) and minor axis (b) of the best-fit ellipse. A state of tension (or compression) was indicated if the wound area was greater (or smaller) than that of the punch (with diameter d). If the wound remained circular (that is, if the anisotropy index $b/a \rightarrow 1$), a state of isotropic stress was identified; elliptical wounds, alternatively, indicated anisotropic stress.

Tissue labeling and tracking

Tissue deformations were quantified by tracking the motion of material point markers. Ectodermal cells were labeled using the lipophilic fluorescent dyes DiI and DiO (Molecular Probes), which incorporate into the cell membrane. Embryos at HH stage 5 ($n=6$) were placed dorsal side

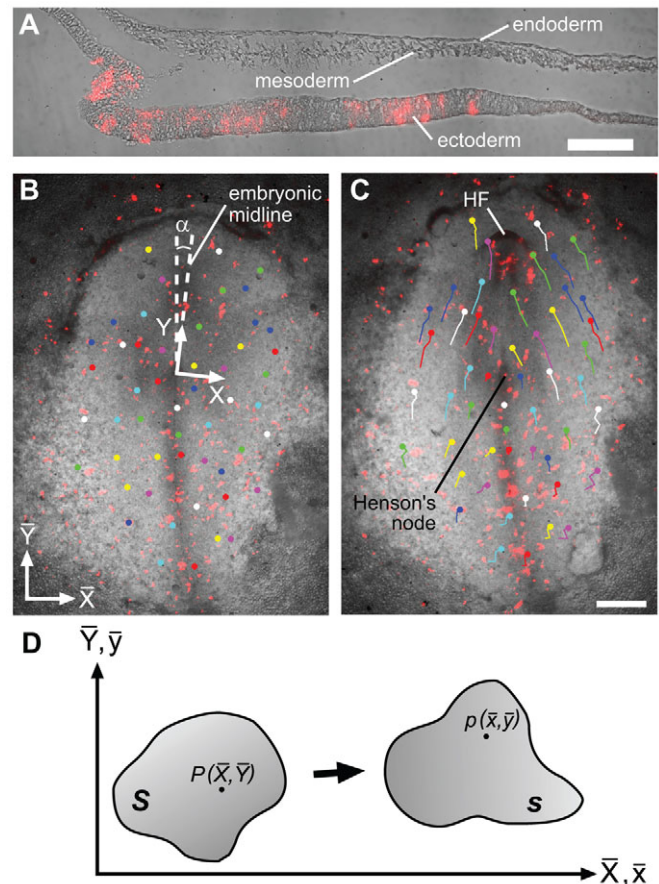


Fig. 2. Quantification of tissue deformation during HF morphogenesis using tracked tissue labels. (A) Parasagittal section (10 μm) of HH stage 6 chick embryo. The ectoderm was labeled with fluorescent dye at HH stage 5, cultured ex ovo until the HF had formed, and then fixed for paraffin sectioning. The fluorescent label was not present in any endodermal or mesodermal cells, confirming that any cells labeled using this technique reside in the ectoderm. Scale bar: 100 μm . (B, C) Fluorescently labeled embryo at HH stage 5 (B) and stage 6 (C). The motion of labeled cells was tracked in image coordinates (\bar{X} , \bar{Y}). Representative label tracks are shown. An embryo coordinate system (X , Y), oriented transverse (X) and parallel (Y) to the embryonic midline and centered at Henson's node, was used to compute Lagrangian strains (α , the angle between the \bar{Y} and Y axes). Scale bar: 500 μm . (D) Deformation of a 2D surface. The point $P(\bar{X}, \bar{Y})$ on surface S deforms into the point $p(\bar{x}, \bar{y})$ on surface s .

up in 35-mm culture dishes and covered with PBS. Glass needles were used to remove the VM and expose the ectoderm. Iron particles, soaked in saturated DiI (or DiO) at room temperature, were then sprinkled across the embryo. After 10 minutes at 38°C, a strong magnet was used to remove the particles, leaving fluorescently labeled cells behind. Using this technique, hundreds of cells could be easily (and simultaneously) labeled.

We repeated this protocol on another embryo using CellTracker CM-DiI (Molecular Probes) to ensure that only cells in the ectoderm were being labeled (Fig. 2A). This fluorescent marker persists after processing for paraffin sections, so the embryo was fixed in 4% paraformaldehyde, embedded in paraffin, and sliced into 10 μm parasagittal sections.

Initial bright-field and fluorescent images of whole embryos were captured using a Leica DMLB microscope and attached video camera (Retiga 1300). Embryos were then cultured until the HF had formed at HH stage 6, ~2–4 hours later. Subsequent time-lapse images were captured at ~30- to 45-minute intervals. The motion of labeled cells was tracked using the Manual

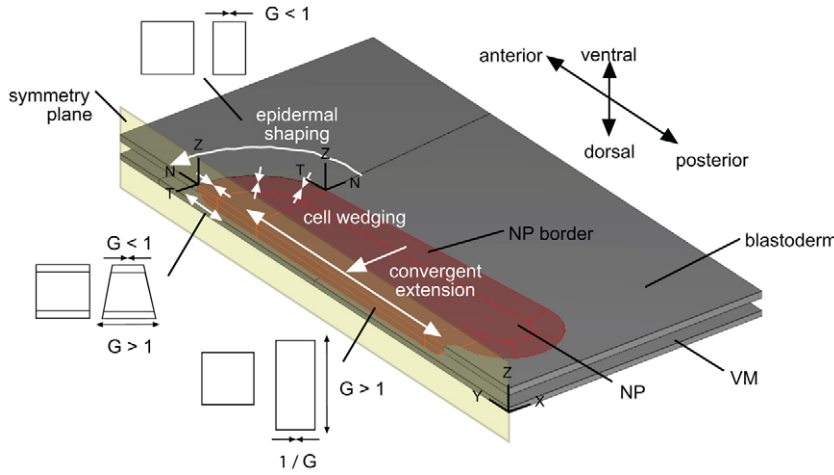


Fig. 3. Computational model of HF formation.

The model geometry consists of the blastoderm and VM separated by a narrow interstitial space. A plane of symmetry is specified along the embryonic midline, and frictionless mechanical contact between the blastoderm and VM is assumed. The growth tensor \mathbf{G} drives morphogenesis in the model. Cell wedging along the anterior border of the NP, convergent extension of the NP, and epidermal shaping outside the NP were simulated by specifying the growth components $G_i(t)$ in each active region (schematics and white arrows). See main text for details.

Tracking plug-in in ImageJ (Fig. 2B,C), and the positions of selected labels were recorded in image coordinates (\bar{X}, \bar{Y}) at each time point, where the origin of the \bar{X}, \bar{Y} system is the lower left corner of the camera frame and \bar{X} and \bar{Y} are the horizontal and vertical coordinate axes, respectively.

Strain analysis

Tissue marker coordinates were used to calculate morphogenetic strains. Briefly, consider a planar surface S that deforms into the planar surface s (Fig. 2D), where the point $P(\bar{X}, \bar{Y})$ on S moves to the location $p(\bar{x}, \bar{y})$ on s . There is a one-to-one mapping between each point on S and s , giving $\bar{x} = \bar{x}(\bar{X}, \bar{Y})$ and $\bar{y} = \bar{y}(\bar{X}, \bar{Y})$. Lagrangian strains characterize the deformation from S to s and are referred to basis vectors in the reference configuration (i.e. S). In image coordinates (\bar{X}, \bar{Y}) , they are defined as:

$$\begin{aligned} E_{\bar{X}\bar{X}} &= \frac{1}{2} \left[\left(\frac{\partial \bar{x}}{\partial \bar{X}} \right)^2 + \left(\frac{\partial \bar{y}}{\partial \bar{X}} \right)^2 - 1 \right] \\ E_{\bar{Y}\bar{Y}} &= \frac{1}{2} \left[\left(\frac{\partial \bar{x}}{\partial \bar{Y}} \right)^2 + \left(\frac{\partial \bar{y}}{\partial \bar{Y}} \right)^2 - 1 \right] \\ E_{\bar{X}\bar{Y}} &= \frac{1}{2} \left[\frac{\partial \bar{x}}{\partial \bar{X}} \frac{\partial \bar{x}}{\partial \bar{Y}} + \frac{\partial \bar{y}}{\partial \bar{X}} \frac{\partial \bar{y}}{\partial \bar{Y}} \right] \end{aligned} \quad (1)$$

The first image in each time-lapse stack (corresponding to HH stage 5) was taken as the reference configuration. As described by Filas et al. (Filas et al., 2007), the MATLAB routine *gridfit* was used to fit 2D surfaces through the set of marker coordinates to generate $\bar{x}(\bar{X}, \bar{Y})$ and $\bar{y}(\bar{X}, \bar{Y})$, which give the strain components in image coordinates by equation (1). Standard equations (Taber, 2004) were then used to transform these strains into components relative to an embryo coordinate system (X, Y) (Fig. 2B), which is oriented transverse (X) and parallel (Y) to the embryonic midline.

Statistics

To analyze our wound geometry data, a two-level nested ANOVA with the Tukey post-hoc test was implemented in a spreadsheet (Sokal and Rohlf, 1981; Zar, 2010). Circular statistics were used to characterize wound orientation (Zar, 2010).

Computational methods

Finite element model

To study the mechanical forces that drive HF formation, we constructed a nonlinear (large deformation), 3D finite element (FE) model using COMSOL Multiphysics (Version 3.4, COMSOL AB, Providence, RI, USA). As shown below, contact between the embryonic blastoderm and VM is an important factor. Hence, the model geometry consists of the blastoderm and VM separated by a narrow interstitial space (Fig. 3) and a plane of symmetry is specified along the midline. Frictionless contact between the blastoderm and VM is assumed, with an augmented Lagrangian approach used to solve for the contact pressure. Consistent with our OCT images of HF-stage embryos (see below), the NP is twice as thick as the surrounding epithelium.

To model the mechanics of morphogenesis, we use the theory of Rodríguez et al. (Rodríguez et al., 1994) to simulate finite volumetric growth. The main idea is that the total deformation of a pseudoelastic body, described by the deformation gradient tensor \mathbf{F} , can be decomposed into a growth tensor \mathbf{G} and an elastic deformation gradient tensor \mathbf{F}^* via the relation $\mathbf{F} = \mathbf{F}^* \cdot \mathbf{G}$. During growth, \mathbf{G} changes the zero-stress configuration of each material element, while \mathbf{F}^* generates stress and enforces geometric compatibility between elements. This theory has been used to model a number of morphogenetic processes (Taber, 2001; Taber, 2008). An introductory treatment can be found in section 3 of Taber (Taber, 1995).

To model anisotropic growth, two coordinate systems are defined (Fig. 3). The first is the global embryo coordinate system (X, Y, Z) , where the X and Y axes coincide with the transverse and longitudinal embryonic axes, respectively. The second is a local curvilinear coordinate system (N, T, Z) , defined such that the N and T axes are oriented to be normal and tangent, respectively, to the NP border (and thus to the prospective HF). We assume that growth occurs along orthogonal directions defined by the unit vectors $\mathbf{e}_1, \mathbf{e}_2$ and \mathbf{e}_3 , which are rooted in the reference configuration with $(1, 2, 3) = (X, Y, Z)$ or (N, T, Z) . The growth tensor thus has the form $\mathbf{G} = G_1 \mathbf{e}_1 \mathbf{e}_1 + G_2 \mathbf{e}_2 \mathbf{e}_2 + G_3 \mathbf{e}_3 \mathbf{e}_3$, where the G_i are growth stretch ratios. As discussed below, the components of \mathbf{G} are specified functions of time in each active region of the model.

Mechanical properties

Tissue stress depends on the elastic deformation \mathbf{F}^* through the material constitutive relations. As a first approximation, embryonic tissues can be treated as pseudoelastic materials (Zamir et al., 2003; Zamir and Taber, 2004a; Zamir and Taber, 2004b) with viscoelastic material effects (e.g. stress relaxation) ignored. The blastoderm and VM are thus modeled as isotropic sheets of nearly incompressible material, characterized by the modified neo-Hookean strain-energy density function:

$$W = \frac{\mu}{2} (\bar{I}^* - 3) + p \left(1 - J^* - \frac{p}{2\kappa} \right), \quad (2)$$

where μ is the small-strain shear modulus, κ is the bulk modulus, $J^* = \det \mathbf{F}^*$ is the elastic dilatation ratio, p is a penalty variable introduced for nearly incompressible materials, and $\bar{I}^* = J^{*-2/3} \text{tr}(\mathbf{F}^{*T} \cdot \mathbf{F}^*)$ is a modified strain invariant. In terms of W , the Cauchy stress tensor is given (Taber, 2004) as:

$$\boldsymbol{\sigma} = J^{*-1} \mathbf{F}^* \cdot \frac{\partial W}{\partial \mathbf{F}^{*T}}. \quad (3)$$

Microindentation tests in our laboratory have suggested that the bending rigidity (stiffness) of the NP (D_{NP}) is approximately twice that of the surrounding epithelium (D_S) (V.D.V., unpublished). The bending rigidity of a linear elastic plate is given by $D = Eh^3/12(1-\nu^2)$, where E is the elastic modulus, h is the plate thickness and ν is Poisson's ratio (Timoshenko and Woinowsky-Krieger, 1959). Inputting thickness values for the NP and surrounding epithelium based on our OCT images, this solution yields $E_S \approx 2E_{NP}$, which gives $\mu_S \approx 2\mu_{NP}$ as μ is linearly related to E . Other

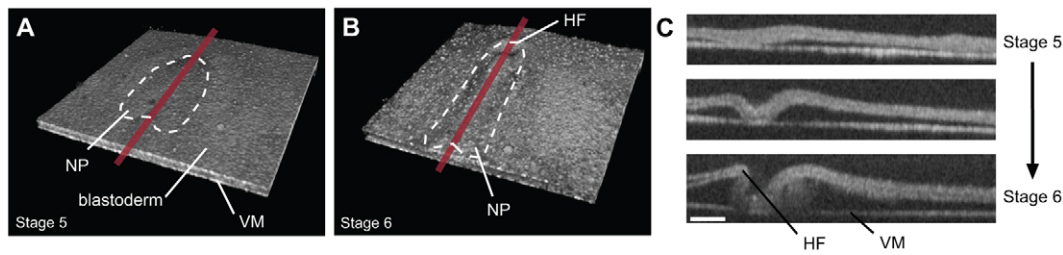


Fig. 4. OCT reveals 3D HF geometry in living embryos. (A,B) Three-dimensional OCT reconstructions of the developing chick embryo at HH stage 5 (A) and stage 6 (B). The imaging window is 2 mm square. (C) Optical midline sections (red lines in A,B) show the blastoderm doubling over on itself and contacting the VM as the HF forms. Scale bar: 200 μm .

microindentation experiments (V.D.V., unpublished) have shown the VM to be approximately three times stiffer than the NP, which (following a similar process) gives $\mu_{VM} \approx 100\mu_{NP}$.

Simulation of morphogenetic processes

The growth tensor \mathbf{G} drives morphogenesis in our model. The growth components $G_i(t)$ for each active region were selected by manual iteration. Parameter values were rejected if the model did not qualitatively match the observed HF morphology, as well as the measured stress and strain distributions in normal embryos. The selected $G_i(t)$ were further tested using data from mechanically perturbed embryos. Our proposed mechanism for HF formation consists of three main morphogenetic processes (Fig. 3), as described below.

Active cell wedging

Actively generated, wedge-shaped cells have often been implicated in epithelial invaginations (Ettensohn, 1985; Haigo et al., 2003). In the chick embryo, Lawson et al. (Lawson et al., 2001) have reported cell wedging along the NP border, a phenomenon that appears intrinsic to the NP border zone and thus independent of any external loads (Moury and Schoenwolf, 1995). We model this wedging along the anterior NP border by specifying $G_N < 1$ along the ventral side of the blastoderm and $G_N > 1$ along the dorsal side, where N is the direction normal to the border (Fig. 3). This changes a cuboidal element into a wedge-shaped element. Cytoskeletal contraction has been linked to cell wedging (Lee and Nagele, 1985; Gorfinkel et al., 2009; Martin et al., 2009) and, moreover, microindentation data from our laboratory suggest that the HF stiffens as it forms (V.D.V., unpublished). A concomitant material stiffening thus accompanies our simulated wedging (i.e. μ_{NP} increases by a factor of 5).

Convergent extension

During neurulation, the NP elongates longitudinally and shortens transversely, a process known as convergent extension (Smith and Schoenwolf, 1997; Colas and Schoenwolf, 2001; Ezin et al., 2009). This behavior appears intrinsic to the NP itself and has been attributed to both cell intercalation (Schoenwolf and Alvarez, 1989; Ezin et al., 2009) and coordinated cell division (Sausedo et al., 1997). The mitotic cycle of neuroepithelial cells at this stage of development lasts ~8–12 hours (Schoenwolf, 1994). Since HF formation occurs over a shorter time period (typically 2–4 hours), we assume cell intercalation is the dominant process and model convergent extension by specifying $G_X < 1$ and $G_Y = 1/G_X$ in the NP (Fig. 3). No change in material properties accompanies this growth, and the components of \mathbf{G} specify an isochoric deformation (i.e. no volume change), as we are concerned solely with cell rearrangement.

Epidermal shaping

The epidermal (or non-neuroepithelial) ectoderm undergoes autonomous changes in shape during neurulation (Moury and Schoenwolf, 1995). In particular, the epidermis anterior to the NP (and thus, the prospective HF) narrows transversely. We model this epidermal shaping by specifying $G_T < 1$ along the blastoderm anterior to the NP, where T indicates the direction tangent to the NP border (Fig. 3).

Finally, our hole-punching experiments (see below) have shown that the blastoderm is in a state of equibiaxial tension before the HF forms. We therefore apply initial equibiaxial tensile stresses along the peripheral boundary of the blastoderm. The magnitude of this tension is based on experimental estimates of the amount of stretch in the tissue.

RESULTS

HF geometry is distinctly three dimensional

During the first day of development, the chick blastoderm is organized as a flat, laminar disk (Patten, 1971). It is composed of three separate germ layers (endoderm, mesoderm and ectoderm) and underlies the VM. During these early stages, there are few visible landmarks to distinguish the embryonic body from the surrounding extra-embryonic tissues (Lillie, 1952). At 24 hours of incubation, however, a conspicuous crescent-shaped fold (the HF) forms at the anterior end of the thickened NP, where the blastoderm transitions to a thinner epithelium (Fig. 1).

Using our time-lapse OCT system, we generated 3D images of the developing HF in living embryos (Fig. 4A,B). Optical sections along the embryonic midline showed that, as the HF forms, the blastoderm bends locally at the NP border, contacts the VM, and doubles over onto itself (Fig. 4C). The tissue is tucked into an S-shaped configuration, with the HF lifted above the plane of the surrounding blastoderm.

Isolated ectoderm creates an HF

Our proposed mechanism for HF morphogenesis involves active forces generated in the ectoderm. To establish whether ectoderm alone can produce an HF, we cultured isolated ectoderm from HH stage 5 (pre-HF) embryos (Fig. 5). Within 2 hours, these explants developed an HF (Fig. 5C), suggesting that the forces that create this structure are of ectodermal origin.

Tissue deformation is inhomogeneous and anisotropic

We used ectodermal cell displacements to characterize the kinematic behavior of the blastoderm during HF formation. Fluorescent labels were tracked as in dynamic fate mapping studies (Redkar et al., 2001; Cui et al., 2009; Ezin et al., 2009). Here, however, the goal was to quantify the global deformation of the tissue, rather than determine the eventual fate of individual cells.

Tracking the motion of tissue labels, we computed 2D Lagrangian strain distributions during HF formation (Fig. 6). During this process, most of the blastoderm remains relatively flat, so 2D Lagrangian strains can be used to capture the salient kinematic behavior outside the immediate HF region. The strain components E_{XX} and E_{YY} characterize relative length changes of

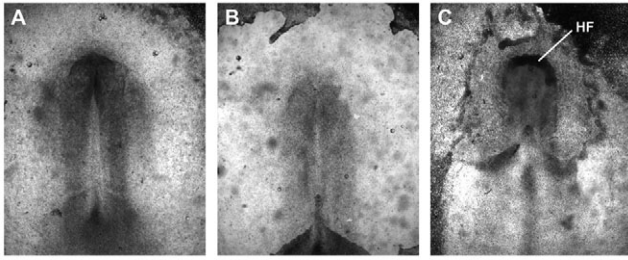


Fig. 5. Forces that create the HF are ectodermal in origin. The ectoderm was isolated in a group of HH stage 5 chick embryos ($n=6$). (A) Representative embryo before treatment, (B) immediately after dissection of endoderm and mesoderm, and (C) after incubation for 2 hours. Isolated ectodermal explants still developed an HF.

line elements originally oriented parallel to the X and Y axes, respectively; E_{XY} is a measure of angle changes between originally normal line elements.

Strain distributions (measured for HH stage 6 relative to stage 5) were inhomogeneous and anisotropic, but remained relatively symmetric about the embryonic midline (Fig. 6). Negative transverse strains were present near the HF, and the shear distribution was primarily organized as a pair of bilateral peaks that spanned the lateral NP border. Meanwhile, the NP elongated longitudinally ($E_{YY}>0$) and shortened transversely ($E_{XX}<0$). At intermediate time points, the overall strain patterns were remarkably similar; only the component magnitudes varied in time (V.D.V., unpublished).

Stress inhomogeneity and anisotropy develop as the HF forms

We estimated the stress distribution in the blastoderm at different stages of development by excising circular plugs of tissue and measuring the resultant hole geometry immediately after wounding

(Fig. 7). With a and b being the major and minor axes of the ellipse fit to a given wound, we computed the wound area, anisotropy index (b/a) and orientation (direction of the major axis). Wound geometry was compared with that of the circular punching pipette of diameter d .

At stage 4, before either the HF had formed or NP had elongated, the wounds were relatively circular, $\sim 45\%$ larger than the punching pipette, and similarly sized both inside and outside the NP (black and red holes/bars in Fig. 7B,E,F). These data indicate that the blastoderm is initially in a state of approximately uniform, isotropic tension.

As the HF formed (at stage 6), the stresses in the blastoderm became markedly non-uniform and anisotropic (other colors in Fig. 7D,E,F). Outside the NP, wound size increased dramatically, indicating a significant rise in tension from that at stage 4. Moreover, anterior to the NP (Fig. 7, blue), this state of increased tension was anisotropic, as revealed by the wounds becoming more elliptical (b/a reduced). Along the NP border (Fig. 7, green), the wounds were smaller ($\sim 78\%$ of the size of the punching pipette) and indicated the presence of compressive stresses. Here again, the elliptical shape of the wounds connoted a definite anisotropy to the stresses in this region. In the middle of the NP (Fig. 7, purple), however, the wound size was similar to that at stage 4 ($\sim 28\%$ larger than the pipette area) and revealed a relatively constant, tensile stress state.

We used wound orientation to characterize the direction of anisotropy. Anterior to the NP, a dominant line of tension was oriented along the transverse embryonic axis (Fig. 7D,G). Meanwhile, along the NP border, the anisotropy was oriented oblique to the border, as indicated by the anterior slant of the wounds in this region (Fig. 7D,H).

The model captures HF geometry during normal development

As discussed in the Materials and methods, our computational model consists of two flat plates, corresponding to the blastoderm and VM, separated by a narrow interstitial space (Fig. 3). The

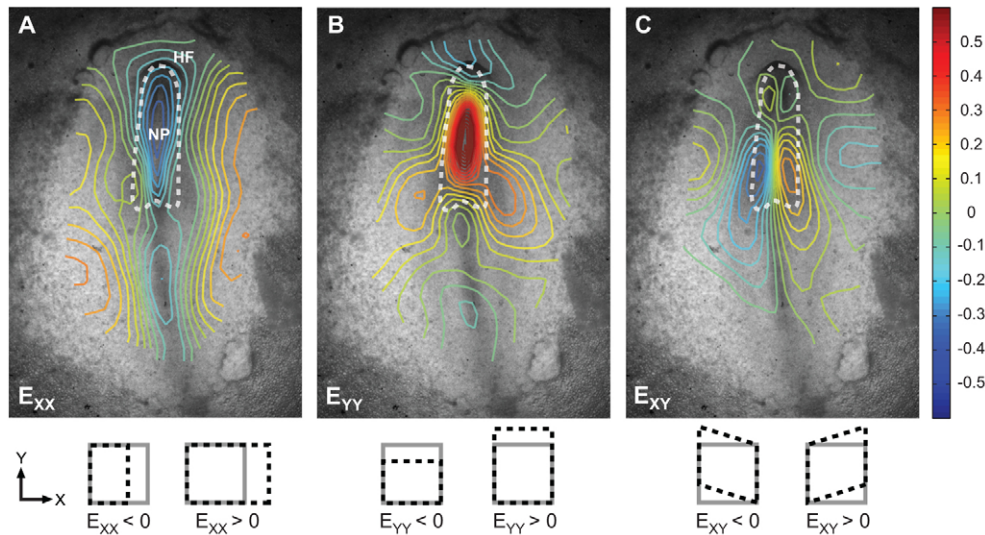


Fig. 6. Measured morphogenetic strain distributions are inhomogeneous. Lagrangian strain contours were calculated for HH stage 6 relative to stage 5. (A,B) Transverse (E_{XX}) (A) and longitudinal (E_{YY}) (B) strains characterize the length changes of line elements originally oriented along the X and Y axes, respectively. (C) The shear strains (E_{XY}) correspond to angle changes between line elements. Each distribution was non-uniform and relatively symmetric about the embryonic midline. Contours from a representative embryo ($n=5$) are shown. The NP (indicated by dashed line) elongated longitudinally ($E_{YY}>0$) and shortened transversely ($E_{XX}<0$), whereas the normal strains near the HF were negative ($E_{XX}<0$ and $E_{YY}<0$). A local peak in shear overlapped the lateral NP border.

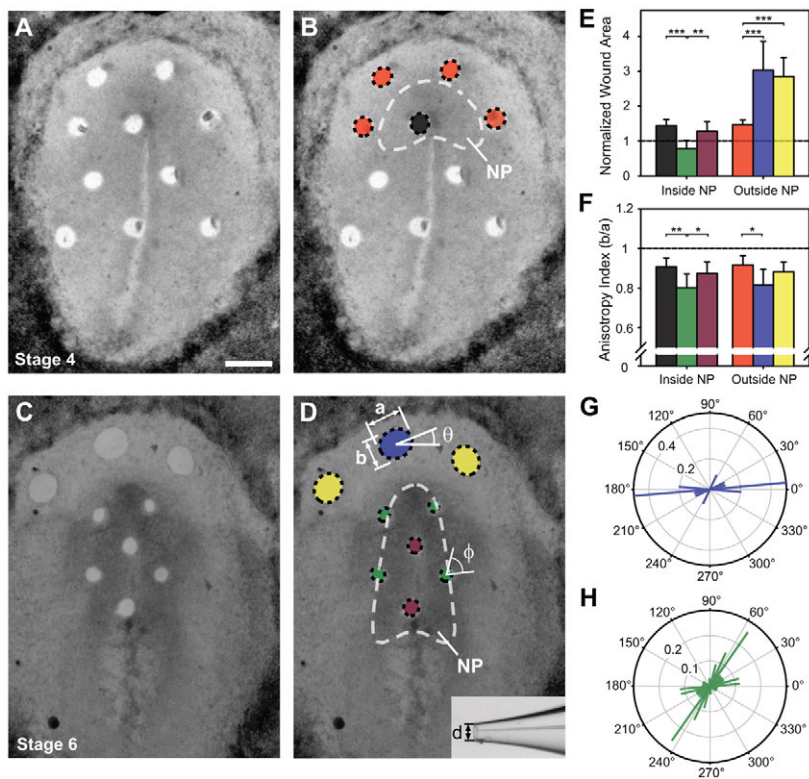


Fig. 7. Stress anisotropy develops as the HF forms. (A–D) Hole punching experiment of (A,B) HH stage 4 and (C,D) stage 6 chick embryo. Note that A and B are the same image, as are C and D. Wound geometry was used to estimate regional tissue stress. Best-fit ellipses were computed for each wound with major and minor elliptical axes a and b , respectively. Wound area and anisotropy index (b/a) were compared with that of the circular punching pipette of diameter d (D, inset). Scale bar: 500 μm . At stage 4: red, outside NP; black, inside NP. At stage 6: blue, anterior to HF; yellow, lateral to HF; green, NP border; purple, middle NP. θ , angle measured from transverse embryonic (or X) axis; ϕ , angle measured from normal to NP border. (E,F) Quantitation of (E) wound area (normalized to the area of the pipette) and (F) anisotropy index both inside and outside the NP, as indicated. Black, $n=3$; red, $n=3$; blue, $n=9$; yellow, $n=7$; green, $n=9$; purple, $n=4$. * $P<0.05$, ** $P<0.01$, *** $P<0.001$ (nested ANOVA with Tukey post-hoc test). Error bars indicate \pm standard deviation (G,H) Relative frequency circular histograms of wound orientation anterior to the HF (G) and along the NP border (H) in stage 6 embryos. The 95% confidence intervals for (G) θ and (H) ϕ were $10\pm14^\circ$ and $43\pm11^\circ$, respectively. At stage 4, the blastoderm is approximately in a state of isotropic, uniform tension. During HF formation, however, the mechanical stresses become markedly anisotropic and non-uniform, especially anterior to the HF and along the NP border.

simulation includes three morphogenetic processes: (1) convergent extension of the NP; (2) cell wedging along the anterior NP border; and (3) autonomous epidermal shaping anterior to the NP.

The magnitudes of the driving forces, i.e. the components of the growth tensor \mathbf{G} , were determined using data from normal embryos (see Fig. S1 in the supplementary material). With these values, the model produces a characteristic crescent-shaped HF (Fig. 8A and see Movie 1 in the supplementary material), and a midline section through the model shows the HF raised above the plane of the surrounding blastoderm as observed in experiments (Fig. 8B and see Movie 2 in the supplementary material). All three morphogenetic processes, which occur simultaneously in the embryo, are required (Fig. 8C). The model solution is fairly robust; variations of up to 33% in the growth parameters do not drastically modify the deformed geometry (see Fig. S2 in the supplementary material). This solution, however, is not necessarily unique. Thus, to strengthen our confidence in the model, we tested it using additional experimental data.

The model qualitatively matches measured strain distributions

Global changes in shape do not uniquely characterize the kinematics of a deforming body, as multiple strain patterns can produce the same overall change in shape. So, to further test the model, we compared strain distributions given by the model with our experimental strain data (Fig. 9). For consistency with the experimental strains, 2D numerical strains were calculated by considering only displacements parallel to the XY plane. Both model and experimental strains are computed with respect to the initially stretched configuration at stage 5.

The strain fields were in reasonable agreement qualitatively (Fig. 9), as both showed transverse shortening ($E_{XX}<0$) and longitudinal elongation ($E_{YY}>0$) in the NP, as well as shortening in both directions anterior to the NP ($E_{XX}<0$ and $E_{YY}<0$). Moreover, the

model predicted the continuous shear strains (E_{XY}) across the NP border, as well as the local peak near the border. The model, however, did not capture all of the striking spatial patterns seen experimentally, namely the mediolateral E_{XX} gradient (Fig. 9).

The model captures experimental anisotropy in tissue stress

We also compared the stresses in the model with the results from our hole punching experiments. The eigenvalues and eigenvectors of the Cauchy stress tensor $\boldsymbol{\sigma}$ specify the principal stresses (σ_1, σ_2) and principal stress directions, respectively, and provide a coordinate-invariant description of the stress state at each material point. We computed normalized principal Cauchy stresses ($\bar{\sigma}_{1,2}=\sigma_{1,2}/\mu_S$) to identify regions of tension and compression in the model. Because each hole was punched through the full thickness of the blastoderm, all model stresses were averaged across the thickness of the membrane.

Consistent with our hole punching experiments (Fig. 7B), an initial equibiaxial tension was specified along the boundary of the model blastoderm, yielding a normalized isotropic pre-stress of 0.22 within the NP and 0.43 in the surrounding epithelium. After the HF formed, principal stress distributions given by the model showed qualitative agreement with our hole punching data (Fig. 10A,B). As in experiments, the model predicted compressive stresses along the NP border and anterior NP, and captured the strongly tensile stresses outside the NP.

We also used the computed principal stress distributions to simulate our hole punching protocol. At points corresponding to experimental wound locations, the principal stresses were extracted from the HF model and imported into a relatively simple plane-stress model, consisting of a square membrane composed of the same material. The imported principal stresses were specified along the membrane edges, and a circular hole was introduced at the center of the stretched membrane to

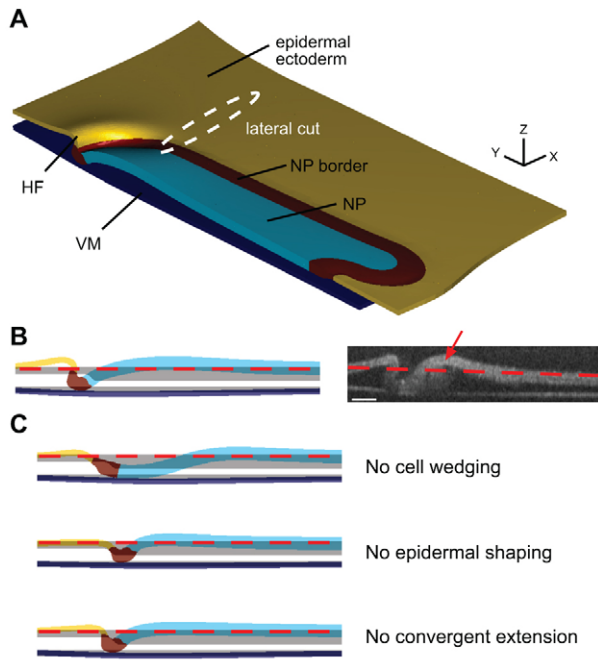


Fig. 8. Model captures normal HF morphology. (A) The deformed model geometry has a characteristically crescent-shaped HF. (B) A midline section of the model (left) shows the HF lifted above the plane of the surrounding material (red dashed line) and captures the key geometrical features seen experimentally via OCT (right). The model, however, was unable to completely reproduce the local curvature in the blastoderm just posterior to the HF (red arrow). The gray (shadowed) section indicates the undeformed model geometry. Scale bar: 200 μm . (C) Removing any one of our morphogenetic forces alters the simulated HF geometry.

simulate wounding. The deformed wound geometry was compared with that of experiments, and principal stress directions in the HF model were compared with experimental measures of wound orientation. Further details for such a model can be found in Varner and Taber (Varner and Taber, 2010).

The sizes and shapes of the holes given by this method qualitatively matched the wound geometries from our hole punching experiments (Fig. 10B). For example, anterior to the HF, the simulated wound indicated a state of anisotropic tension similar to that seen experimentally (Fig. 10B). Moreover, the predicted dominant line of tension, oriented along the transverse embryonic (or X) axis, also matched that determined by our experiments (Fig. 10C). The model also captured the anisotropic compression observed along the NP border, although the hole was oriented nearly normal to the NP border, not oblique as observed experimentally (Fig. 10D).

The model predicts abnormal morphology when development is perturbed

Mechanical perturbations were used to test the predictive capabilities of the model. Our OCT images (Fig. 4C) suggest that contact with the VM constrains the deformation of the blastoderm as it folds. To determine its role in shaping the HF, we removed the VM from stage 5 embryos and followed their development for 2-3 hours of culture. Midline sections revealed abnormal HF geometry, with the fold being less sharp and the HF no longer elevated above the plane of the surrounding blastoderm (Fig. 11A).

We simulated this experiment by removing the VM in the model, without changing any of the other model parameters. The predicted morphology was similar to that seen in our OCT images (Fig. 11E, middle row), although the V-shaped blastoderm was not as symmetric in the model as in the actual embryo.

In a separate set of experiments, we altered the stress field in the tissue by cutting through the lateral blastoderm (outside the NP) in embryos that had already formed an HF (Fig. 11B-D). These linear cuts relieved the stress at these locations, and the opening of the wounds indicated a state of tension consistent with our punch experiments (Fig. 7D). OCT images showed that, immediately after cutting, the HF began to unfurl (Fig. 11B,C). After an hour of incubation (Fig. 11D), the HF had unfolded even further, indicating a vital morphogenetic role for the tension outside the NP.

To model this experiment, a lateral incision was simulated by removing a thin, elliptic cylindrical volume of material from the blastoderm (Fig. 8A). The simulation was then run with none of the model parameters modified. The predicted shape of the

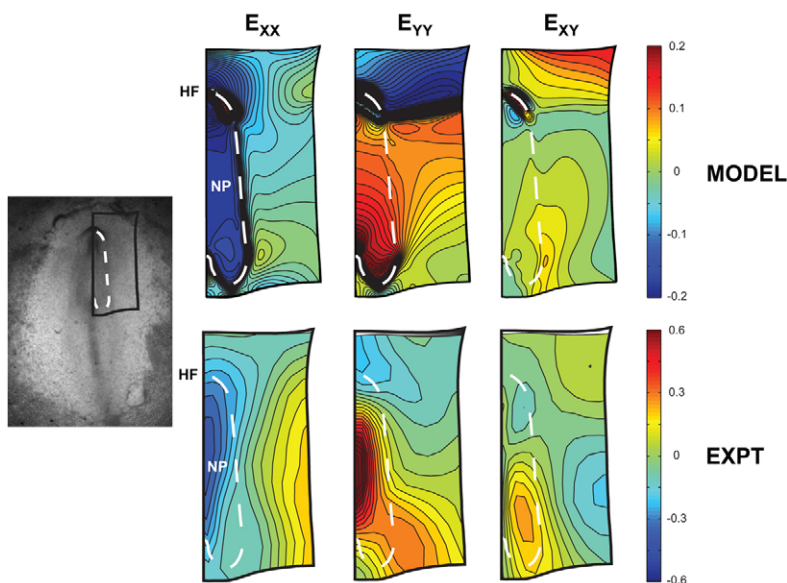


Fig. 9. Numerical strain fields qualitatively match experiments. Transverse (E_{xx}), longitudinal (E_{yy}) and shear (E_{xy}) strain contours were computed in the model and compared with our experimental strain data (see Fig. 6). The strain fields are in reasonable agreement. Both show $E_{xx} < 0$ and $E_{yy} > 0$ in the NP, and $E_{xx} < 0$ and $E_{yy} < 0$ anterior to the NP. The model also predicts continuous E_{xy} across the NP border and the local E_{xy} peak near the border.

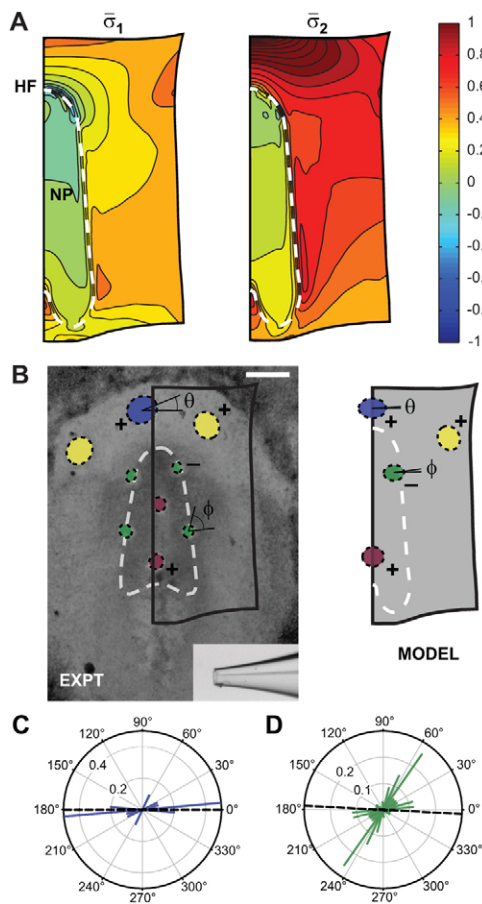


Fig. 10. Model predicts anisotropy in tissue stress. The principal stresses in the model agree qualitatively with the results of our hole punching experiments. **(A)** Normalized principal Cauchy stress contours ($\bar{\sigma}_{1,2} = \sigma_{1,2}/\mu_s$) given by the model indicate strongly tensile and anisotropic stresses anterior to the HF, compressive stresses along the anterior NP and NP border, and a nearly isotropic tensile stress state in the posterior NP. **(B)** Simulations of our hole punching experiments predict similar wound shapes (see Fig. 7). Blue, anterior to HF; yellow, lateral to HF; green, NP border; purple, middle NP. The plus and minus symbols indicate tension and compression, respectively. **(C,D)** Simulated wound orientation data anterior to the HF (C) and along the NP border (D) were compared with experimental results. The model predicts a dominant line of tension anterior to the HF at $\theta = 0^\circ$ (dashed black line in C), similar to the $\theta = 10 \pm 14^\circ$ observed experimentally (blue bars). Along the NP border, the simulation gives $\phi = -3^\circ$ (dashed black line in D), whereas in experiments $\phi = 43 \pm 11^\circ$ (green bars).

blastoderm was remarkably similar to that in the treated embryos, as the invagination was V-shaped with the HF being much less prominent and remaining close to the plane of the embryo (Fig. 11E, bottom row).

Taken together, these results show that our model captures the fundamental mechanical behavior of the embryo during HF formation. The ability of the model to predict the abnormal tissue geometries encountered during mechanical perturbations offers further support for our proposed morphogenetic mechanisms.

DISCUSSION

The mechanical forces that shape developing tissues have long intrigued embryologists. In fact, before the introduction of modern genetic and molecular techniques, much of the language used to

describe morphogenesis was decidedly mechanical in nature (Bellairs, 1953; Stalsberg and DeHaan, 1968; Patten, 1971; Ettensohn, 1985). Although this biophysical thinking about embryogenesis largely fell out of favor in the 1970s and 1980s, recent work has begun to connect our accumulated genetic and molecular understanding of development with physical morphogenetic mechanisms (Davidson, 2008; Lecuit, 2008; Wozniak and Chen, 2009; Zhou et al., 2009). New progress on the mechanics of morphogenesis is being made in the study of *Drosophila* dorsal closure (Blanchard et al., 2009; Gorfinkel et al., 2009; Solon et al., 2009) and germ band extension (Rauzi et al., 2008; Blanchard et al., 2009), avian gastrulation (Zamir et al., 2006), amphibian neurulation (Chen and Brodland, 2008), cardiac looping (Taber, 2006; Ramasubramanian et al., 2008), and vertebrate convergent extension (Davidson et al., 2009; Zhou et al., 2009).

Here, we propose a new hypothesis for the mechanics of HF formation. As discussed below, our hypothesis is based on experimental studies going back more than a century.

The need for a new hypothesis

The HF is a crucial, yet somewhat overlooked, event in morphogenesis. Besides its role in initiating neurulation, the HF is closely linked to the formation of the primitive foregut and heart tube in both chick (Bellairs and Osmond, 2005) and human (Moore et al., 2000; Oostra et al., 2007). In particular, the HF creates the rudimentary foregut pocket (Lillie, 1952; Bellairs, 1953; Schoenwolf and Smith, 2000) and serves as the initial site of fusion for the precardiac epithelia (Stalsberg and DeHaan, 1969; Wei et al., 2001; Moreno-Rodriguez et al., 2006). The out-of-plane bending of the blastoderm convects and rotates the heart fields into their proper ventral position, enabling them to form a tube along the ventral aspect of the embryo (Drake and Jacobson, 1988; de la Cruz and Sanchez-Gomez, 1998; Slack, 2006; Abu-Issa and Kirby, 2008). The importance of the HF to these processes was convincingly demonstrated in the classic experiment by DeHaan, in which a simple incision through the HF disrupted both heart field fusion and foregut formation (DeHaan, 1959).

HF formation was, in fact, one of the very first morphogenetic processes to draw the attention of early embryologists. As early as 1881, in his seminal *Treatise on Comparative Embryology*, Francis Balfour described the avian HF as a “tucking in” of the blastoderm, a description that seemed to suggest a role for active folding of the tissue (Balfour, 1881; Foster and Balfour, 1883). A few years later, Shore and Pickering explicitly challenged this idea, proposing instead that differential growth drives HF morphogenesis (Shore and Pickering, 1889). Specifically, they posited that the embryonic area of the blastoderm grows faster than the surrounding extra-embryonic area; the blastoderm then buckles out of plane to form the HF as the embryonic area “[grows] forwards... over the portion of the area pellucida which lies in front of it”. In their view, this alternative hypothesis explained away the role for any active folding or tucking in of the tissue. In addition, consistent with our own findings (Fig. 4C, Fig. 11E), the authors speculated that mechanical contact with the VM plays a role in shaping the HF.

In the mid-twentieth century, Stalsberg and DeHaan (Stalsberg and DeHaan, 1968), building on work by Bellairs (Bellairs, 1953), suggested a different buckling mechanism. They proposed that regression of Henson’s node pulls the embryonic midline (i.e. the NP or Shore and Pickering’s embryonic area) downward, causing the blastoderm to buckle and roll over the fixed anterior border of the NP. This folding forms the HF and initiates foregut development.

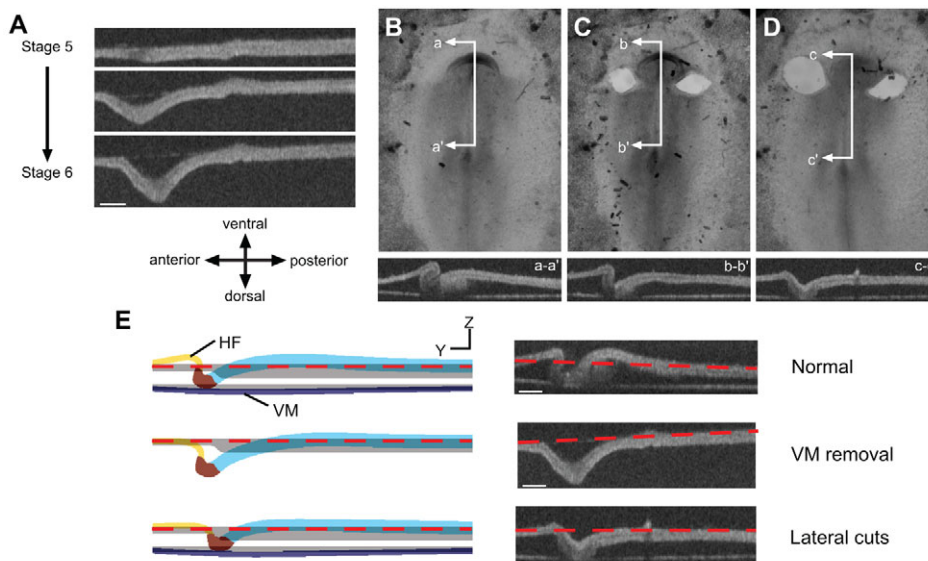


Fig. 11. Effect of mechanical perturbations on HF morphology.

(A) Midline time-lapse OCT sections of chick embryo after removal of the VM at HH stage 5 ($n=3$). (B–D) Linear cuts in lateral blastoderm ($n=4$) reveal tensile stress state. Midline OCT sections before treatment (B, a–a'), immediately after cutting (C, b–b'), and after 1 hour incubation (D, c–c'), show the HF progressively unfurling. (E) Simulating each of these perturbations by eliminating the VM (middle row) and removing a thin, elliptical cylindrical volume of lateral blastoderm (bottom row, see Fig. 8A) produced similarly abnormal tissue geometries. Scale bars: 200 μm .

Their buckling mechanism, however, is inconsistent with our experiment in which an HF develops without a direct connection to Henson's node (see Fig. S3 in the supplementary material). We thus propose a new hypothesis for HF formation that includes many of the active ectodermal processes that shape the neural tube. Specifically, we postulate that (1) active cell wedging at the NP border, (2) convergent extension of the NP, and (3) epidermal shaping anterior to the NP generate the mechanical forces that drive this process. This hypothesis is motivated by the following experimental results.

First, Lawson et al. demonstrated that localized cell wedging accompanies the epithelial bending (or kinking) that occurs along the NP border (Lawson et al., 2001), and this behavior appears intrinsic to the border zone itself (Moury and Schoenwolf, 1995). The cellular mechanisms that drive this wedging, however, have yet to be determined, but might include actomyosin contraction (Gorfinkel et al., 2009; Martin et al., 2009), interkinetic nuclear migration (Smith and Schoenwolf, 1988; Schenk et al., 2009), or laminin-dependent basal constriction (Gutzman et al., 2008).

Second, it has also been well established that the NP elongates by convergent extension (Smith and Schoenwolf, 1997; Colas and Schoenwolf, 2001; Ezin et al., 2009). External loads may play a role in this process, but that role appears to be a subsidiary one, as convergent extension occurs within NP isolates (Moury and Schoenwolf, 1995) and has been attributed to both cell intercalation (Schoenwolf and Alvarez, 1989; Ezin et al., 2009) and coordinated cell division (Sausedo et al., 1997).

Third, the epidermal ectoderm anterior to the NP actively shortens in the transverse direction (Moury and Schoenwolf, 1995). Although the cellular mechanisms behind this epidermal shaping are still unclear, there is evidence that coordinated cell division plays a role. The orientation of these dividing cells (i.e. the direction along which tissue growth occurs) might depend on mechanical stress (Sausedo et al., 1997).

Computational models help elucidate morphogenetic forces

We have integrated computational modeling and in vitro experiments to determine the tissue-level forces that drive HF formation. In highly nonlinear problems (such as this one), physical

intuition can often be misleading, and models are a useful tool, enabling us to quantitatively investigate whether a given hypothesis is consistent with physical law.

Morphological and mechanical experiments can be used to test the model. However, in problems of morphogenesis, it is important to note that matching global tissue geometry does not guarantee a unique solution, and other types of experiments (e.g. stress, strain) can be used to test the model more rigorously.

To test our hypothesis for HF formation, we constructed a 3D computational model that consists of two pseudoelastic plates corresponding to the blastoderm and VM. A continuum mechanics framework is used because we are concerned here with tissue-level deformations. The model geometry, material constants and boundary conditions are all based on experimental observations in normal chick embryos. We used 3D OCT reconstructions, morphogenetic strain distributions and qualitative stress estimates to test the model and identify reasonable values for the free parameters (i.e. the components of \mathbf{G}) that determine the magnitude of the hypothesized driving forces.

The model matches the HF geometry observed in living embryos using OCT (Figs 4 and 8). Although it captures the key geometrical features, the model does not, however, reproduce the local curvature in the blastoderm just posterior to the HF (Fig. 8B, arrow). One reason for this discrepancy might be our assumption of uniform growth (i.e. convergent extension) in the NP, as there is some evidence that the extent of cell rearrangement varies along the embryonic midline (Schoenwolf and Alvarez, 1989). Alternatively, apical constriction of median hinge-point cells along the midline (Lee and Nagele, 1985; Colas and Schoenwolf, 2001) might further enhance this local curvature.

The model also qualitatively matches our morphogenetic strain data (Fig. 9), which, consistent with existing data on avian convergent extension, show the NP elongating longitudinally ($E_{YY} > 0$) and shortening transversely ($E_{XX} < 0$) (Schoenwolf and Sheard, 1989; Smith and Schoenwolf, 1997; Colas and Schoenwolf, 2001; Ezin et al., 2009). Moreover, in both the model and experiments, the negative transverse strains (E_{XX}) surrounding the HF are in agreement with previously reported evidence of epidermal shaping (Moury and Schoenwolf, 1995), and the shear strains (E_{XY}), akin to the reorientation movements described by Ezin et al. (Ezin et al., 2009), are the result of NP growth being

constrained by surrounding tissue. Interestingly, the difference in material properties between the NP and surrounding tissue (that is, between μ_{NP} and μ_S) is such that the shear strains are continuous across the NP border.

A lack of complete agreement between the strain distributions given by the model and our experimental data could be attributed to the model geometry or to our assumption of uniform growth. In the model, the thickness of the blastoderm is uniform outside the NP; however, transverse OCT sections indicate that the thickness of the blastoderm decreases towards the periphery of the embryo (V.D.V., unpublished). This could contribute to the laterally increasing E_{XX} gradient observed in experiments (Fig. 9), as the thinner (lateral) material would deform to a greater extent under the stresses exerted by the narrowing NP. Alternatively, the effects of non-uniform growth could also be a factor.

To our knowledge, this work constitutes the first study of mechanical stress in HF-stage chick embryos. Before HF morphogenesis, the blastoderm is in a state of uniform, isotropic tension; as the HF forms, however, the stress distribution becomes both inhomogeneous and anisotropic (Fig. 7). Our model effectively captures this non-uniform stress field (Fig. 10), predicting both compressive and tensile stresses in the NP, and large tensile stresses in the blastoderm surrounding it. In addition, the model predicts the dominant line of tension observed anterior to the HF (Fig. 10C).

Lastly, to gauge the predictive capability of the model, we simulated two mechanical perturbation experiments that disrupted the normal stress field: lateral cutting of the blastoderm and VM removal. Strikingly, the model reasonably captures the abnormal tissue geometry in both cases (Fig. 11E).

The HF is shaped by forces typically associated with neurulation

These results suggest that our hypothesized morphogenetic mechanisms, which include those typically associated with neurulation, are the primary driving forces behind HF formation. Given its central importance to both heart tube and foregut formation, a more complete biophysical understanding of this crucial morphogenetic event should provide insight into how embryonic tissues are organized during early cardiac development.

By characterizing the forces that shape the HF during normal development, future work can be undertaken to determine how molecular or genetic perturbations mechanically disrupt this process. In mice, for example, inactivation of the Huntington's disease gene *Hdh* (*Htt* – Mouse Genome Informatics) disrupts early embryonic patterning and completely blocks HF formation (Duyao et al., 1995; Woda et al., 2005). How this aberrant patterning influences the morphogenetic forces that shape the HF remains unclear. Other results provide further evidence of a link between head and heart development. In chick, Rho kinase (ROK) expression is enriched in the HF, and inhibition of ROK, which is implicated in cytoskeletal organization, often generates embryos with cardia bifida, particularly if the inhibitor is applied before the HF has formed (Wei et al., 2001). Here again, the biophysical consequences of this perturbation are unknown and warrant further attention.

The integrated use of quantitative modeling and experiments is well suited to answer these questions, and the approach presented here can be readily generalized to other morphogenetic processes, offering us a chance to understand how physical forces are organized at the tissue level to create biological form.

Acknowledgements

We thank the members of the L.A.T. laboratory for insightful comments, Stephanie Lindsey for help with the microindentation experiments and Dr Igor Efimov (Washington University) for use of the OCT imaging system. This work was supported by grants R01 GM075200 and R01 HL083393 from the National Institutes of Health (L.A.T.), and grant 09PRE2060795 from the American Heart Association (V.D.V.). Deposited in PMC for release after 12 months.

Competing interests statement

The authors declare no competing financial interests.

Supplementary material

Supplementary material for this article is available at <http://dev.biologists.org/lookup/suppl/doi:10.1242/dev.054387/-DC1>

References

- Abu-Issa, R. and Kirby, M. L. (2008). Patterning of the heart field in the chick. *Dev. Biol.* **319**, 223–233.
- Balfour, F. M. (1881). *A Treatise on Comparative Embryology*. London: Macmillan.
- Bellairs, R. (1953). Studies on the development of the foregut in the chick blastoderm: 2. The morphogenetic movements. *J. Embryol. Exp. Morphol.* **1**, 369–385.
- Bellairs, R. and Osmond, M. (2005). *The Atlas of Chick Development*. London: Elsevier.
- Blanchard, G. B., Kabla, A. J., Schultz, N. L., Butler, L. C., Sanson, B., Gorfinkel, N., Mahadevan, L. and Adams, R. J. (2009). Tissue tectonics: morphogenetic strain rates, cell shape change and intercalation. *Nat. Methods* **6**, 458–464.
- Chen, X. and Brodland, G. W. (2008). Multi-scale finite element modeling allows the mechanics of amphibian neurulation to be elucidated. *Phys. Biol.* **5**, 15003.
- Clark, A. G., Miller, A. L., Vaughan, E., Yu, H. Y., Penkert, R. and Bement, W. M. (2009). Integration of single and multicellular wound responses. *Curr. Biol.* **19**, 1389–1395.
- Colas, J. F. and Schoenwolf, G. C. (2001). Towards a cellular and molecular understanding of neurulation. *Dev. Dyn.* **221**, 117–145.
- Cui, C., Cheuvront, T. J., Lansford, R. D., Moreno-Rodriguez, R. A., Schultheiss, T. M. and Rongish, B. J. (2009). Dynamic positional fate map of the primary heart-forming region. *Dev. Biol.* **332**, 212–222.
- Davidson, L. A. (2008). Integrating morphogenesis with underlying mechanics and cell biology. *Curr. Top. Dev. Biol.* **81**, 113–133.
- Davidson, L. A., Joshi, S. D., Kim, H. Y., von Dassow, M., Zhang, L. and Zhou, J. (2009). Emergent morphogenesis: elastic mechanics of a self-deforming tissue. *J. Biomech.* **43**, 63–70.
- Davies, J. A. (2005). *Mechanisms of Morphogenesis*. Amsterdam: Elsevier.
- de la Cruz, M. V. and Sanchez-Gomez, C. (1998). Straight heart tube. Primitive cardiac cavities vs. primitive cardiac segments. In *Living Morphogenesis of the Heart* (ed. M. V. de la Cruz and R. R. Markwald), pp. 85–98. Boston: Birkhauser.
- DeHaan, R. L. (1959). Cardia bifida and the development of pacemaker function in the early chick heart. *Dev. Biol.* **1**, 586–602.
- Desprat, N., Supatto, W., Pouille, P. A., Beaurepaire, E. and Farge, E. (2008). Tissue deformation modulates twist expression to determine anterior midgut differentiation in Drosophila embryos. *Dev. Cell* **15**, 470–477.
- Drake, C. J. and Jacobson, A. G. (1988). A survey by scanning electron microscopy of the extracellular matrix and endothelial components of the primordial chick heart. *Anat. Rec.* **222**, 391–400.
- Duyao, M. P., Auerbach, A. B., Ryan, A., Persichetti, F., Barnes, G. T., McNeil, S. M., Ge, P., Vonsattel, J. P., Gusella, J. F., Joyner, A. L. et al. (1995). Inactivation of the mouse Huntington's disease gene homolog *Hdh*. *Science* **269**, 407–410.
- Ettensohn, C. A. (1985). Mechanisms of epithelial invagination. *Q. Rev. Biol.* **60**, 289–307.
- Ezin, A. M., Fraser, S. E. and Bronner-Fraser, M. (2009). Fate map and morphogenesis of presumptive neural crest and dorsal neural tube. *Dev. Biol.* **330**, 221–236.
- Farge, E. (2003). Mechanical induction of Twist in the Drosophila foregut/stomodaeal primordium. *Curr. Biol.* **13**, 1365–1377.
- Filas, B. A., Efimov, I. R. and Taber, L. A. (2007). Optical coherence tomography as a tool for measuring morphogenetic deformation of the looping heart. *Anat. Rec.* **290**, 1057–1068.
- Filas, B. A., Knutsen, A. K., Bayly, P. V. and Taber, L. A. (2008). A new method for measuring deformation of folding surfaces during morphogenesis. *J. Biomech. Eng.* **130**, 061010.
- Foster, M. and Balfour, F. M. (1883). *The Elements of Embryology*. London: Macmillan.
- Fujimoto, J. G. (2003). Optical coherence tomography for ultrahigh resolution in vivo imaging. *Nat. Biotechnol.* **21**, 1361–1367.
- Gorfinkel, N., Blanchard, G. B., Adams, R. J. and Martinez Arias, A. (2009). Mechanical control of global cell behaviour during dorsal closure in Drosophila. *Development* **136**, 1889–1898.

- Gutzman, J. H., Graeden, E. G., Lowery, L. A., Holley, H. S. and Sive, H. (2008). Formation of the zebrafish midbrain-hindbrain boundary constriction requires laminin-dependent basal constriction. *Mech. Dev.* **125**, 974-983.
- Haigo, S. L., Hildebrand, J. D., Harland, R. M. and Wallingford, J. B. (2003). Shroom induces apical constriction and is required for hinge point formation during neural tube closure. *Curr. Biol.* **13**, 2125-2137.
- Hamburger, V. and Hamilton, H. L. (1951). A series of normal stages in the development of the chick embryo. *J. Morphol.* **88**, 49.
- Huang, D., Swanson, E. A., Lin, C. P., Schuman, J. S., Stinson, W. G., Chang, W., Hee, M. R., Flotte, T., Gregory, K. and Puliafito, C. A. (1991). Optical coherence tomography. *Science* **254**, 1178-1181.
- Hutson, M. S., Tokutake, Y., Chang, M. S., Bloor, J. W., Venakides, S., Kiehart, D. P. and Edwards, G. S. (2003). Forces for morphogenesis investigated with laser microsurgery and quantitative modeling. *Science* **300**, 145-149.
- Joshi, S. D., von Dassow, M. and Davidson, L. A. (2010). Experimental control of excitable embryonic tissues: three stimuli induce rapid epithelial contraction. *Exp. Cell Res.* **316**, 103-114.
- Lawson, A., Anderson, H. and Schoenwolf, G. C. (2001). Cellular mechanisms of neural fold formation and morphogenesis in the chick embryo. *Anat. Rec.* **262**, 153-168.
- Lecuit, T. (2008). 'Developmental mechanics': cellular patterns controlled by adhesion, cortical tension and cell division. *HFSP J.* **2**, 72-78.
- Lee, H. Y. and Nagele, R. G. (1985). Studies on the mechanisms of neurulation in the chick: interrelationship of contractile proteins, microfilaments, and the shape of neuroepithelial cells. *J. Exp. Zool.* **235**, 205-215.
- Lillie, F. R. (1952). *Development of the Chick: an Introduction to Embryology*. New York: Holt.
- Martin, A. C., Kaschube, M. and Wieschaus, E. F. (2009). Pulsed contractions of an actin-myosin network drive apical constriction. *Nature* **457**, 495-499.
- Moore, K. L., Persaud, T. V. N. and Shiota, K. (2000). *Color Atlas of Clinical Embryology*. Philadelphia, PA: Saunders.
- Moreno-Rodriguez, R. A., Krug, E. L., Reyes, L., Villavicencio, L., Mjaatvedt, C. H. and Markwald, R. R. (2006). Bidirectional fusion of the heart-forming fields in the developing chick embryo. *Dev. Dyn.* **235**, 191-202.
- Moury, J. D. and Schoenwolf, G. C. (1995). Cooperative model of epithelial shaping and bending during avian neurulation: autonomous movements of the neural plate, autonomous movements of the epidermis, and interactions in the neural plate/epidermis transition zone. *Dev. Dyn.* **204**, 323-337.
- Oostra, R. J., Steding, G., Lamers, W. H. and Moorman, A. F. (2007). *Steding's and Viragh's Scanning Electron Microscopy Atlas of the Developing Human Heart*. New York, Berlin: Springer.
- Patten, B. M. (1971). *Early Embryology of the Chick*. New York: McGraw-Hill.
- Ramasubramanian, A., Nerurkar, N. L., Achtien, K. H., Filas, B. A., Voronov, D. A. and Taber, L. A. (2008). On modeling morphogenesis of the looping heart following mechanical perturbations. *J. Biomech. Eng.* **130**, 061018.
- Rauzi, M., Verant, P., Lecuit, T. and Lenne, P. F. (2008). Nature and anisotropy of cortical forces orienting *Drosophila* tissue morphogenesis. *Nat. Cell Biol.* **10**, 1401-1410.
- Redkar, A., Montgomery, M. and Litvin, J. (2001). Fate map of early avian cardiac progenitor cells. *Development* **128**, 2269-2279.
- Rodriguez, E. K., Hoger, A. and McCulloch, A. D. (1994). Stress-dependent finite growth in soft elastic tissues. *J. Biomech.* **27**, 455-467.
- Sausedo, R. A., Smith, J. L. and Schoenwolf, G. C. (1997). Role of nonrandomly oriented cell division in shaping and bending of the neural plate. *J. Comp. Neurol.* **381**, 473-488.
- Schenk, J., Wilsch-Brauninger, M., Calegari, F. and Huttner, W. B. (2009). Myosin II is required for interkinetic nuclear migration of neural progenitors. *Proc. Natl. Acad. Sci. USA* **106**, 16487-16492.
- Schoenwolf, G. C. (1994). Formation and patterning of the avian neuraxis: one dozen hypotheses. *Ciba Found. Symp.* **181**, 25-50.
- Schoenwolf, G. C. and Alvarez, I. S. (1989). Roles of neuroepithelial cell rearrangement and division in shaping of the avian neural plate. *Development* **106**, 427-439.
- Schoenwolf, G. C. and Sheard, P. (1989). Shaping and bending of the avian neural plate as analysed with a fluorescent-histochemical marker. *Development* **105**, 17-25.
- Schoenwolf, G. C. and Smith, J. L. (2000). Gastrulation and early mesodermal patterning in vertebrates. *Methods Mol. Biol.* **135**, 113-125.
- Shore, T. W. and Pickering, J. W. (1889). The proamnion and amnion in the chick. *J. Anat. Physiol.* **24**, 1-21.
- Slack, J. M. W. (2006). *Essential Developmental Biology*. Oxford: Blackwell.
- Smith, J. L. and Schoenwolf, G. C. (1988). Role of cell-cycle in regulating neuroepithelial cell shape during bending of the chick neural plate. *Cell Tissue Res.* **252**, 491-500.
- Smith, J. L. and Schoenwolf, G. C. (1997). Neurulation: coming to closure. *Trends Neurosci.* **20**, 510-517.
- Sokal, R. R. and Rohlf, F. J. (1981). *Biometry: the Principles and Practice of Statistics in Biological Research*. San Francisco: W. H. Freeman.
- Solon, J., Kaya-Copur, A., Colombelli, J. and Brunner, D. (2009). Pulsed forces timed by a ratchet-like mechanism drive directed tissue movement during dorsal closure. *Cell* **137**, 1331-1342.
- Stalsberg, H. and DeHaan, R. L. (1968). Endodermal movements during foregut formation in the chick embryo. *Dev. Biol.* **18**, 198-215.
- Stalsberg, H. and DeHaan, R. L. (1969). The precardiac areas and formation of the tubular heart in the chick embryo. *Dev. Biol.* **19**, 128-159.
- Taber, L. A. (1995). Biomechanics of growth, remodeling, and morphogenesis. *Appl. Mech. Rev.* **48**, 487-545.
- Taber, L. A. (2001). Biomechanics of cardiovascular development. *Annu. Rev. Biomed. Eng.* **3**, 1-25.
- Taber, L. A. (2004). *Nonlinear Theory of Elasticity: Applications in Biomechanics*. River Edge, NJ: World Scientific.
- Taber, L. A. (2006). Biophysical mechanisms of cardiac looping. *Int. J. Dev. Biol.* **50**, 323-332.
- Taber, L. A. (2008). Theoretical study of Belousov's hyper-restoration hypothesis for mechanical regulation of morphogenesis. *Biomech. Model. Mechanobiol.* **7**, 427-441.
- Timoshenko, S. and Woinowsky-Krieger, S. (1959). *Theory of Plates and Shells*. New York: McGraw-Hill.
- Varner, V. D. and Taber, L. A. (2010). On measuring stress distributions in epithelia. In *IUTAM Symposium on Cellular, Molecular and Tissue Mechanics* (ed. K. Garikipati and E. M. Arruda), pp. 45-54. New York: Springer.
- Voronov, D. A. and Taber, L. A. (2002). Cardiac looping in experimental conditions: effects of extraembryonic forces. *Dev. Dyn.* **224**, 413-421.
- Wei, L., Roberts, W., Wang, L., Yamada, M., Zhang, S., Zhao, Z., Rivkees, S. A., Schwartz, R. J. and Imanaka-Yoshida, K. (2001). Rho kinases play an obligatory role in vertebrate embryonic organogenesis. *Development* **128**, 2953-2962.
- Woda, J. M., Calzonetti, T., Hilditch-Maguire, P., Duyao, M. P., Conlon, R. A. and MacDonald, M. E. (2005). Inactivation of the Huntington's disease gene (Hdh) impairs anterior streak formation and early patterning of the mouse embryo. *BMC Dev. Biol.* **5**, 17.
- Wozniak, M. A. and Chen, C. S. (2009). Mechanotransduction in development: a growing role for contractility. *Nat. Rev. Mol. Cell Biol.* **10**, 34-43.
- Zamir, E. A. and Taber, L. A. (2004a). On the effects of residual stress in microindentation tests of soft tissue structures. *J. Biomech. Eng.* **126**, 276-283.
- Zamir, E. A. and Taber, L. A. (2004b). Material properties and residual stress in the stage 12 chick heart during cardiac looping. *J. Biomech. Eng.* **126**, 823-830.
- Zamir, E. A., Srinivasan, V., Perucchio, R. and Taber, L. A. (2003). Mechanical asymmetry in the embryonic chick heart during looping. *Ann. Biomed. Eng.* **31**, 1327-1336.
- Zamir, E. A., Czirok, A., Rongish, B. J. and Little, C. D. (2005). A digital image-based method for computational tissue fate mapping during early avian morphogenesis. *Ann. Biomed. Eng.* **33**, 854-865.
- Zamir, E. A., Czirok, A., Cui, C., Little, C. D. and Rongish, B. J. (2006). Mesodermal cell displacements during avian gastrulation are due to both individual cell-autonomous and convective tissue movements. *Proc. Natl. Acad. Sci. USA* **103**, 19806-19811.
- Zar, J. H. (2010). *Biostatistical Analysis*. Upper Saddle River, NJ: Prentice-Hall/Pearson.
- Zhou, J., Kim, H. Y. and Davidson, L. A. (2009). Actomyosin stiffens the vertebrate embryo during crucial stages of elongation and neural tube closure. *Development* **136**, 677-688.